Journal of Natural Gas Science and Engineering 24 (2015) 510–517

Contents lists available at ScienceDirect

Journal of Natural Gas Science and Engineering

journal homepage: www.elsevier.com/locate/jngse

Attenuation effects on the seismic response of a bottom-simulating reflector

Ayman Qadrouh [a, b], José M. Carcione [c, *], Ahmed M. Salim [b], Zuhar Zahir Tuan Harith [d]

[a] SAC – KACST, PO Box 6086, Riyadh 11442, Saudi Arabia
[b] Department of Geosciences, Faculty of Petroleum Technology, Universiti Teknologi Petronas, Bandar Seri Iskandar, 31750 Tronoh, Perak, Malaysia
[c] Istituto Nazionale di Oceanografia e di Geofisica Sperimentale (OGS), Borgo Grotta Gigante 42c, 34010 Sgonico, Trieste, Italy
[d] Institute of Petroleum Engineering, Heriot-Watt University Malaysia, Level 2, Menara PjH, No 2 Jalan Tun Abdul Razak, Precinct 2, 62100 Putrajaya, Malaysia

ARTICLE INFO

Article history:
Received 20 February 2015
Received in revised form
10 April 2015
Accepted 11 April 2015
Available online

Keywords:
BSR
Attenuation
Velocity dispersion
Poroelasticity
Modeling

ABSTRACT

Bottom simulation reflectors (BSR) are seismic events generally corresponding to a partially saturated layer with gas separating hydrate-bearing sediments from brine-saturated sediments. Seismic attenuation and velocity dispersion affects the waveform of the BSR event. In this work, we consider a 1D methodology to study the effects of seismic Q, velocity dispersion, layer thickness and properties and characteristics of the overburden on the reflection coefficients and waveform of such event. We describe the media by using a rock-physics model based on poroelasticity, calculate the reflection coefficient of the BSR layer of varying thickness and compute the waveforms with a full-wave pseudospectral method. The proposed rock-physics/modeling methodology is fast in terms of computer requirements and can be used to quantify the seismic properties and compute waveforms useful for seismic interpretation and inversion of quantities such as porosity, hydrate content, gas saturation, clay content and thickness of the BSR layer. We show that in many cases the interpretation can be counterintuitive and a proper rock-physics methodology is essential to reach valid conclusions about the influence of the different parameters on the wave properties.

1. Introduction

Gas hydrates may represent an important source of fuel energy (e.g., Makogon, 2010). The most common detection and quantification technique is seismic surveying. Bottom simulating reflectors on seismic profiles are interpreted to represent the seismic signature of the base of gas hydrate formations overlying a layer partially saturated with free gas. It is observed that the seismic response of the BSR is characterised by low frequencies, called the "low frequency shadow" by Taylor et al. (2000) (see also Geletti and Busetti, 2011). The shift to low frequencies is interpreted as attenuation due to partial saturation with free gas (e.g., Vanneste et al., 2001). However, some caution is required since the presence of low frequencies may be due to other causes, such as NMO stretching, which is important at far offset traces (Dunkin and Levin, 1973). This effect will be investigated in a future work. Here, we focus on intrinsic attenuation by using a 1D model, keeping the description of the physics, while providing a fast and efficient tool for seismic interpretation. Scattering attenuation is not taken into account, since it is important at high (sonic-log) frequencies.

Recently, Dewangan et al. (2014) analysed the effect of gas hydrate and free gas on seismic attenuation. The zones of gas hydrate, identified by the increase in seismic velocity, show high quality factors (Q), a result that agrees with the rock-physics models proposed by Carcione and Tinivella (2000), Gei and Carcione (2003), Carcione and Gei (2004) and Carcione et al. (2005a), and with the experimental results in Rossi et al. (2007). On the other hand, they show that the presence of free gas within the gas hydrate stability zone increases seismic attenuation.

In this work, we study the normal-incidence reflection coefficient of a layer as a function of the layer thickness and quality factor and perform numerical simulation of transient wavefields to obtain the seismic events. The modeling is based on a spectrum of relaxation mechanisms and the differential equations are solved in the space-time domain by using a direct method based on the Fourier

* Corresponding author.
E-mail addresses: aqadrouh@kacst.edu.sa (A. Qadrouh), jcarcione@inogs.it (J.M. Carcione).

http://dx.doi.org/10.1016/j.jngse.2015.04.011
1875-5100/

pseudospectral method (e.g., Carcione, 2015). The media are described by a poroelastic model based on a generalisation of Gassmann equation. In particular, the upper medium containing gas hydrates is a sediment whose skeleton has three phases, namely, quartz, clay and gas hydrate, forming three frames. The model describes also the BSR layer partially saturated with gas as a particular case. To quantify the seismic loss (Q), we use the mesoscopic White model (White, 1975; Carcione, 2015).

Several effects due to wave loss are investigated here. Attenuation in the BSR layer is very low, due to mesoscopic-loss effects because of the presence of gas (e.g., Carcione and Picotti, 2006) and this fact affects the reflection coefficient and the amplitude related to the BSR event. Moreover, the thickness of the BSR layer generates interference effects which also affect the reflection coefficient and the waveform. In order to analyze these phenomena, we compute 1D synthetic seismograms by varying the quality factor and thickness of the BSR layer. In addition, the intrinsic attenuation of the upper layers induces a shift of the spectrum centroid to low frequencies as the traveled distance increases.

Regarding temperature effects as the gas-hydrate stability zone, Gei and Carcione (2003) have compared two empirical equations to ODP data showing a very good agreement. The BSR is deeper for lower geothermal gradients, increasing depth and decreasing temperature of the seafloor. Moreover, temperature and pressure affect the acoustic properties of the fluids, mainly those of the free gas. The relevant equations can be found in Gei and Carcione (2003). In this work, we focus the research on the geometrical and intrinsic attenuation effects. For clarity in reading, we include a list of symbols in Appendix A.

2. Petro-elastical model

Fig. 1 shows the media (denoted by $j = 1,2,3$) and interfaces composing the system, where the BSR event is due to a composite reflection related to layer 2. The sediments above the BSR (medium 1) are saturated with brine containing clay and gas hydrate. This rock can be considered as a composite material with $n = 3$ frames, i.e., the rock (quartz) frame, the clay frame and that of the hydrate network. In the following $i = 1$, 2 and 3 indicate the properties of quartz, clay and gas hydrates, respectively. Carcione et al. (2005b) obtained the wet-rock (Gassmann) bulk modulus of a medium with n frames and one fluid. If ϕ_i is the fraction of the i-th solid and ϕ is the porosity, such that $\sum^{n}\phi_i + \phi = 1$, the Gassmann modulus is

$$K_G = \sum_{i=1}^{n} K_{mi} + \left(\sum_{i=1}^{n} \alpha_i\right)^2 M, \tag{1}$$

where

$$M = \left(\sum_{i=1}^{n} \frac{\phi_i'}{K_i} + \frac{\phi}{K_f}\right)^{-1}, \tag{2}$$

$$\phi_i' = \alpha_i - \beta_i\phi, \quad \alpha_i = \beta_i - \frac{K_{mi}}{K_i}, \quad \beta_i = \frac{\phi_i}{1-\phi}. \tag{3}$$

β_i is the fraction of solid i per unit volume of total solid. Here K_i, $i = 1,\ldots n$ and K_f are the solid and fluid bulk moduli, respectively, and K_{mi}, $i = 1,\ldots n$ are the frame moduli.

A generalization of Krief's model for a multi-mineral porous medium is used to obtain the frame moduli,

$$K_{mi} = (K_{\mathrm{HS}}/v)\beta_i K_i (1-\phi)^{A/(1-\phi)}, \quad i = 1,\ldots,n, \tag{4}$$

where A is a dimensionless parameter, $v = \sum_{i=1}^{n}\beta_i K_i$ is the Voigt average, and $K_{\mathrm{HS}} = (K_+ + K_-)/2$, where K_+ and K_- are the Hashin–Shtrikman (HS) upper and lower bounds (Mavko et al.,

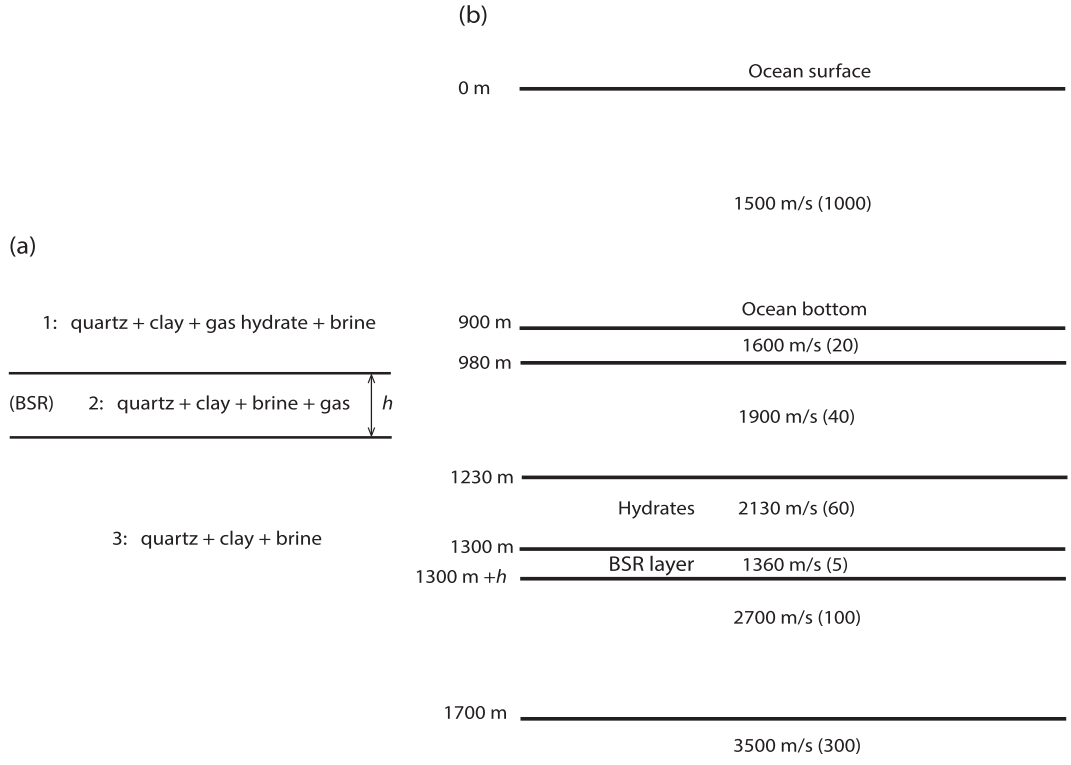

Fig. 1. Geological model. Composition of the BSR system (a) and general model (b). The velocities and quality factors are indicated.

1998; Carcione et al., 2005a,b). The expression (Carcione, 2015) is such that the composite modulus $K_m = \sum^n K_{mi}$ is consistent with the HS bounds when $\phi = 0$.

On the other hand, the dry-rock (and wet-rock) modulus of the composite is

$$\mu_m = \sum_{i=1}^{n} \frac{\mu_i}{K_i} K_{mi}, \tag{5}$$

where μ_i is the rigidity modulus if the i-th solid.

Finally, the P-wave modulus is

$$E = K_G + \frac{4}{3}\mu_m. \tag{6}$$

The model is used to characterise all the media in Fig. 1, to obtain the elastic (lossless velocity) as

$$c = \sqrt{\frac{E}{\rho}}, \tag{7}$$

where ρ is the composite density, given by

$$\rho = (1-\phi)\sum_{i=1}^{n} \beta_i \rho_i + \phi \rho_f, \tag{8}$$

where ρ_i and ρ_f are the densities of the i-th solid phase and fluid, respectively.

Medium 2 has brine and gas in the pores. When the fluids are not mixed in the pore volume, but distributed in patches, the effective bulk modulus of the fluid at high frequencies is higher than that predicted by Wood's model (White, 1975; Mavko et al., 1998; Carcione and Picotti, 2006). To obtain the bulk modulus of the gas–liquid mixture, we use an empirical law introduced by Brie et al. (1995). The effective bulk modulus is given by

$$K_f = (K_b - K_g)S^e + K_g, \tag{9}$$

where K_b and K_g are the brine and gas bulk moduli, S is the brine saturation and e is an empirical parameter. Equation (9) gives Voigt's mixing law for $e = 1$ and an approximation to Wood's model for $e = 40$. The fluid density in this medium is simply given by $\rho_f = S\rho_b + (1-S)\rho_g$, where ρ_b and ρ_g are the brine and gas densities, respectively.

2.1. Anelastic characterisation of the layer

In this case, c becomes complex and frequency dependent in Equation (7). In that equation, c corresponds to the high-frequency limit velocity and E to the unrelaxed modulus E_U. The phase velocity, attenuation factor and quality factor of a viscoelastic medium are

$$c_p = \left[\mathrm{Re}\left(\frac{1}{c}\right)\right]^{-1}, \quad \alpha = -\omega \mathrm{Im}\left(\frac{1}{c}\right) \quad \text{and} \quad Q = \frac{\mathrm{Re}(c^2)}{\mathrm{Im}(c^2)}, \tag{10}$$

respectively, where here c denotes the complex velocity of the P-wave, ω is the angular frequency $\omega = 2\pi f$ and "Re" and "Im" take real and imaginary parts (e.g., Carcione, 2015).

We consider a constant quality factor, $\overline{Q}$, obtained with a spectrum of L Zener relaxation mechanisms, whose peak locations are equispaced in logω scale (see Section 2.4.6 in Carcione (2015)). We then have to find the relaxation times $\tau_{\varepsilon l}$ and $\tau_{\sigma l}$ that gives an almost constant Q in a given frequency band centered at $\omega_{0m} = 1/\tau_{0m}$. This is the location of the mechanism situated at the middle of the band, which, for odd L, has the index $m = L/2 + 1$. The minimum quality factor of the L peaks is the same and is given by

$$Q_0 = \frac{\overline{Q}}{L}\sum_{l=1}^{L} \frac{2\omega_{0m}\tau_{0l}}{1+\omega_{0m}^2\tau_{0l}^2}, \tag{11}$$

where ω_{0m} is defined below and $\omega_{0l} = 1/\tau_{0l}$ are the peak locations. Then, the relaxation times are

$$\tau_{\varepsilon l} = \frac{\tau_{0l}}{Q_0}\left(\sqrt{Q_0^2+1}+1\right) \quad \text{and} \quad \tau_{\sigma l} = \frac{\tau_{0l}}{Q_0}\left(\sqrt{Q_0^2+1}-1\right). \tag{12}$$

If f_0 is the central frequency of the source wavelet, we assume that the centre peak is located at $\omega_{0m} = 2\pi f_0$.

Finally, the complex P-wave modulus is given by

$$E(\omega) = E_U\left(\sum_{l=1}^{L}\frac{\tau_{\varepsilon l}}{\tau_{\sigma l}}\right)^{-1}\sum_{l=1}^{L}\frac{1+\mathrm{i}\omega\tau_{\varepsilon l}}{1+\mathrm{i}\omega\tau_{\sigma l}} \tag{13}$$

(Carcione, 2015; Eq. (2.196)), where E_U is the unrelaxed, high-frequency limit modulus, obtained from the model introduced in the previous section (Equation (7)) and $\mathrm{i} = -1$. If $\omega \to \infty$, $E \to E_U$, Taking into account that $E = \rho c^2$, the quality factor is given by Equation (10).

The cause of the high attenuation in the layer can be due to mesoscopic loss by wave-induced fluid flow (Müller et al., 2010; Carcione, 2015). It is assumed that the medium has patches of gas in a brine saturated background. White's model (White, 1975; Carcione and Picotti, 2006) describes wave velocity and attenuation as a function of frequency, patch size, permeability and viscosity. Attenuation and velocity dispersion are caused by fluid flow between patches of different pore pressures. The critical fluid diffusion relaxation scale is proportional to the square root of the ratio permeability to frequency. At seismic frequencies the length scale is very large, and the pressure is nearly uniform throughout the medium, but as frequency increases, pore pressure differences can cause an important increase in P-wave velocity (Carcione and Picotti, 2006).

3. Reflection coefficient of the BSR

The P-wave reflection coefficient of the layer of thickness h in Fig. 1 is similar to the electromagnetic expression given in Eq. (5.18) of Brekhovskikh (1960) and Section 1.6.4 [Eq. (57)] of Born and Wolf (1964). These authors report the expressions for the transverse-electric (TE) case. TE waves are equivalent to acoustic (P) waves propagating in liquids, while TM waves are equivalent to shear (SH) waves propagating in solids (Carcione and Robinson, 2002). Moreover, the equation in Born and Wolf (1964) is given for purely dielectric media but the lossy version can be obtained by replacing the real dielectric constant by the complex permittivity. Here, we have obtained a complex velocity describing attenuation with the Zener model. The reflection coefficient at normal incidence is

$$R = \frac{r_{12} + r_{23}\exp(-\gamma)}{1 + r_{12}r_{23}\exp(-\gamma)}, \tag{14}$$

where

$$\gamma = \frac{2\mathrm{i}\omega h}{c_2}, \quad r_{12} = \frac{Z_1 - Z_2}{Z_1 + Z_2} \quad \text{and} \quad r_{23} = \frac{Z_2 - Z_3}{Z_2 + Z_3}, \tag{15}$$

where h is the thickness of the layer,

$$Z_j = \rho_j c_j, \quad j = 1, \ldots, 3 \tag{16}$$

is the impedance. The quantity γ is complex and defines the phase (imaginary part) and attenuation (real part) properties of the wave in the layer.

Equation (14) differs from that of Born and Wolf (1964) in the minus sign of the exponent, which arises from the fact that here we use the convention $\exp(+i\omega t)$ instead of $\exp(-i\omega t)$.

In the case in which the media above and below the layer have the same properties, i.e., when $r_{23} = -r_{12} = -r$, Equation (14) becomes

$$R = \frac{r[1 - \exp(-\gamma)]}{1 - r^2 \exp(-\gamma)}. \tag{17}$$

4. Numerical modeling method

The synthetic seismograms are computed with a modeling code based on the viscoacoustic stress–strain relation corresponding to the spectrum of relaxation mechanism introduced in the previous section. The equations are given in Section 2.10.4 of Carcione (2015). The 1D particle velocity-stress formulation for propagation along the z-axis is

$$\begin{aligned} \dot{v}_z &= \frac{1}{\rho}\partial_z \sigma, \\ \dot{\sigma} &= E_U\left(\partial_z v_z + \sum_{l=1}^{L} e_l\right) + s, \\ \dot{e}_l &= \varphi_l \partial_z v_z - \frac{e_l}{\tau_{\sigma l}}, \quad l = 1, \ldots, L, \end{aligned} \tag{18}$$

where v_z is the particle velocity, σ is the stress, s is the source (explosion), e_l are memory variables,

$$\varphi_l = \frac{1}{\tau_{\sigma l}}\left(\sum_{l=1}^{L}\frac{\tau_{\varepsilon l}}{\tau_{\sigma l}}\right)^{-1}\left(1 - \frac{\tau_{\varepsilon l}}{\tau_{\sigma l}}\right). \tag{19}$$

and a dot above a variable denotes time differentiation. The numerical algorithm is based on the Fourier pseudospectral method for computing the spatial derivatives and a 4th-order Runge–Kutta technique for calculating the wavefield recursively in time (e.g., Carcione, 2015).

5. Examples and simulations

The medium properties are shown in Table 1, where the subindices along the first horizontal row denote quartz (1), clay (2) and gas hydrate (3), while the first column indicates the medium as given in Fig. 1. Values of the quality factor as low as 5 can be found in high porosity unconsolidated sediments saturated with gas and can be explained with the mesoscopic attenuation theory. For more details about the model see Carcione et al. (2012). The other properties are: $K_1 = 35$ GPa, $K_2 = 20$ GPa, $K_3 = 8$ GPa, $K_b = 2.4$ GPa, $K_g = 0.007$ GPa, $\mu_1 = 35$ GPa, $\mu_2 = 10$ GPa, $\mu_3 = 3.3$ GPa, $\rho_1 = \rho_2 = 2.65$ g/cm^3, $\rho_3 = 0.92$ g/cm^3, $\rho_b = 1.04$ g/cm^3, $\rho_g = 0.07$ g/cm^3, $S = 91.6\%$ (the gas saturation is 8.4%), $A = 3$ and $e = 20.5$. The unrelaxed P-wave velocities are shown in Table 1, which agree with those of Fig. 9c in Geletti and Busetti (2011). The simulations consider the model shown in Fig. 1. We consider $L = 3$ relaxation mechanisms, with the centre peak located at the source dominant frequency f_p (see below), where the first peak is located at $f_p - 10$ Hz.

Table 1
Medium properties.

Medium	Φ_1	ϕ_2	ϕ_3	ϕ	c [m/s]	ρ [Kg/m^3]	$\overline{Q}$
1	0.34	0.22	0.04	0.4	2130	1937	60
2	0.34	0.22	0	0.44	1360	1906	5
3	0.6	0.05	0	0.35	2700	2086	100

The simulations have 495 grid points with a grid spacing of 5 m. The source $s = \delta(\mathbf{x})g(t)$ has the time history

$$g(t) = \left(u - \frac{1}{2}\right)\exp(-u), \quad u = \left[\frac{\pi(t - t_s)}{T}\right]^2, \tag{20}$$

where T is the period of the wave and $t_s = 1.4\,T$ is a delay to make the wavelet causal. The peak frequency is $f_p = 1/T$. The Runge Kutta algorithm uses a time stepping of 0.5 ms. For simplicity, to avoid reflections from the upper layers, source and receiver are located at 1230 m. In this way, we have the seismic response of the BSR layer without the effects of the overburden.

The normal incidence reflection coefficient versus layer thickness is shown in Fig. 2a and b shows 1D simulations, where the

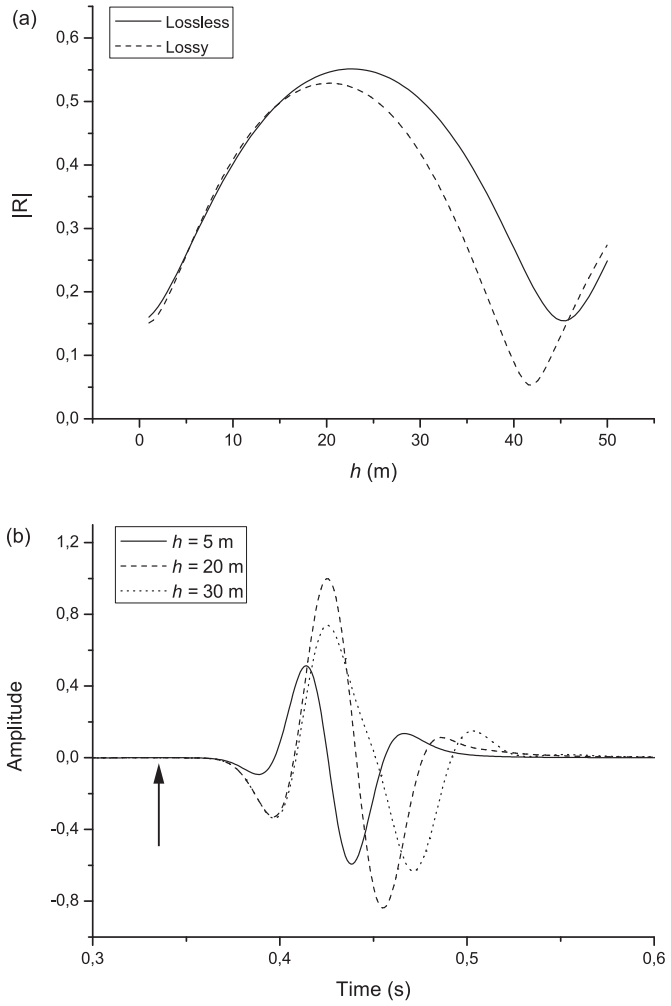

Fig. 2. Normal-incidence reflection coefficient as a function of the layer thickness (a) and 1D simulations (b). The arrow indicates the two-way traveltime of the top of the BSR layer.

source dominant frequency is 15 Hz. The lossless case is also shown, where all the Q factors are infinite. We can see in Fig. 2a that the difference between reflection coefficients of the two cases increases with increasing thickness whereas the difference sharply decrease for a thickness greater than 45 m, and the reflection coefficients for the lossy case is slightly higher than that of the lossless case. The fact that the results present this non-intuitive behaviour means that these type of calculations are important to reveal the physics. In Fig. 2b, the amplitudes of the signal for 5 m and 30 m thickness are comparable, while that corresponding to 20 m is higher, in agreement with the results of Fig. 2a.

Fig. 3 shows other simulations, where we compare the BSR response for different source dominant frequencies (a) and the lossy and lossless cases (b). In the latter case, the source peak frequency is 35 Hz. The thickness of the BSR layer is $h = 30$ m. The time step of the Runge–Kutta algorithm is 1 ms. For 15 Hz a single wavelet can be seen, while the two interfaces of the BSR can be resolved for a 35 Hz dominant frequency. The importance of considering attenuation is evident in Fig. 3b, where the response of the lower interface of the BSR layer is highly attenuated as well as the lower-interface event at 0.65 s generated at 1700 m depth.

According to Table 1, we have considered a hydrate

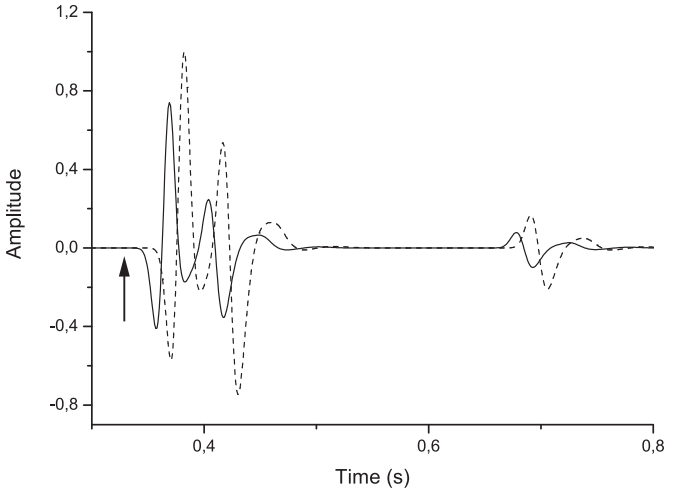

Fig. 4. Comparisons between the seismic responses for hydrate concentrations of 4% (solid line) and 20% (dashed line). The thickness of the layer is $h = 30$ m and the signal frequency is 35 Hz. The arrow indicates the two-way traveltime of the top of the BSR layer.

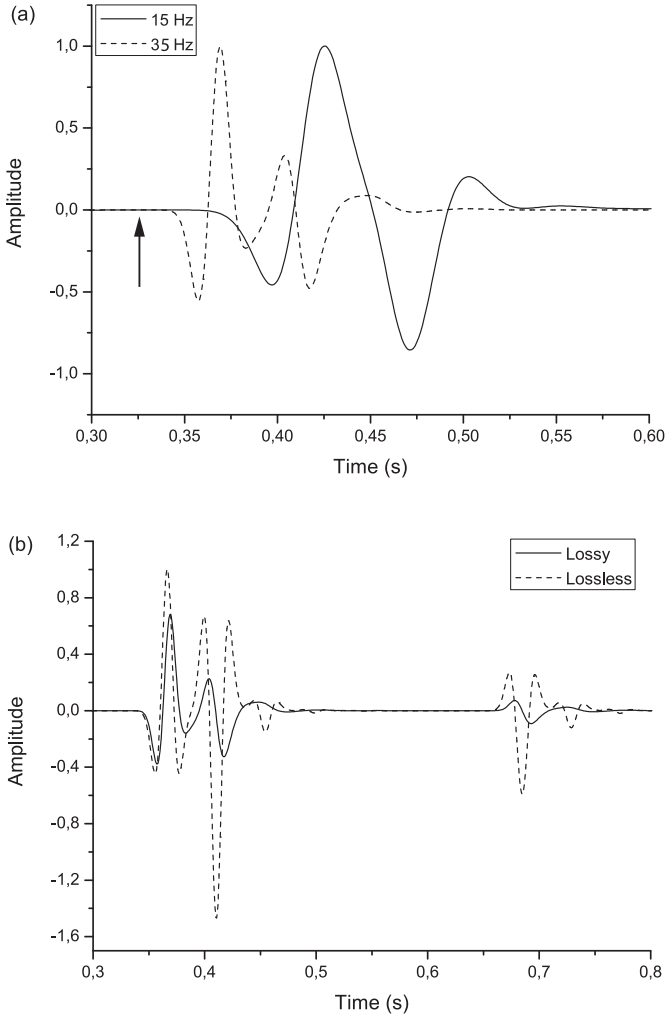

Fig. 3. Comparisons between the seismic responses for different source dominant frequencies (a) and between the lossy and lossless cases ($f_p = 35$ Hz) (b). The thickness of the layer is $h = 30$ m and its quality factor is $Q = 5$. The arrow indicates the two-way traveltime of the top of the BSR layer.

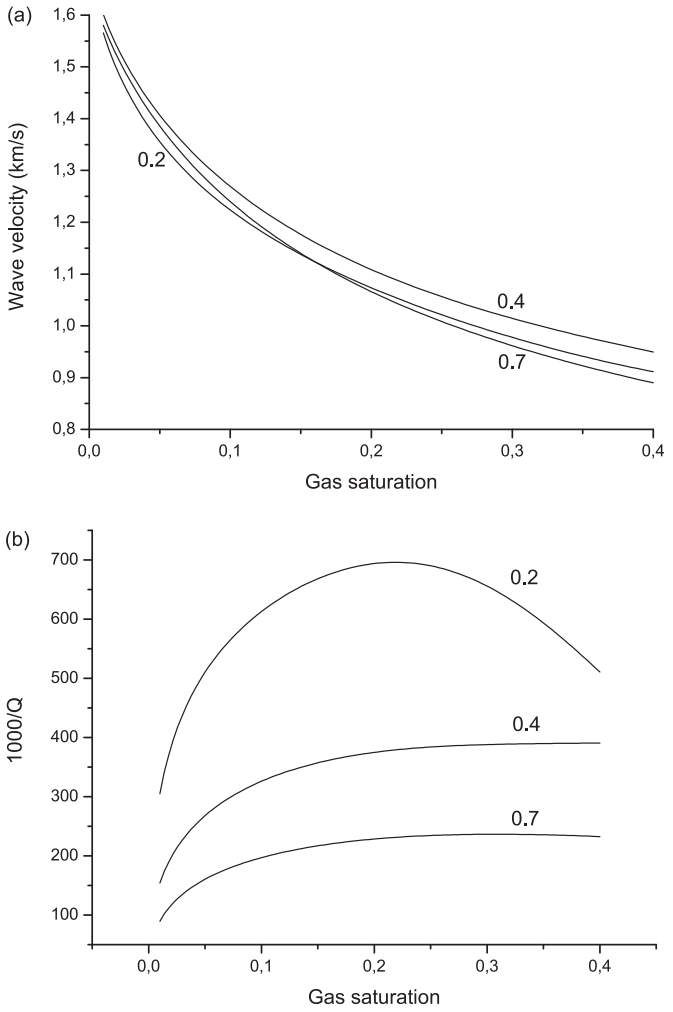

Fig. 5. Wave velocity (a) and quality factor (b) as a function of gas saturation for three values of the clay content $C = \phi_2/(\phi_1 + \phi_2)$.

concentration of 4%. Let us now assume a hydrate concentration of 20%, which gives a velocity of 2050 m/s and a density of 1660 kg/m^3. We kept the same values of clay content, porosity and attenuation. We have assumed the same value of Q for the two concentrations, because the purpose of the calculation is to analyze the effect that the concentration has on the waveforms, which are shown in Fig. 4. As can be seen, the responses of the layer and lower interface are delayed and the amplitude have increased. This plot shows the importance of performing full-wave calculations with the available parameters. Changes in concentration may be confused with Q effects, although in this case there are variations in both arrival time and amplitude of the wavefield.

Next, we assume variations in clay content and saturation in the BSR layer. So far, the Q values have been assumed. In order to model the physics explicitly, we use White's mesoscopic-loss model to obtain realistic values of the velocity and quality factor as a function of clay content and saturation. The equations can be found in Section 2.2 and Appendix A of Carcione et al. (2012). In addition to the values already defined, we assume the viscosities for brine and gas to be $\eta_b = 0.0012$ Pa s and $\eta_g = 0.0002$ Pa s, quartz and clay grains with radii 50 μs and 1 μs, respectively, $A = 3.9$ and gas patches of 10 cm size. The permeability is calculated with Equation (18) of Carcione et al. (2012). Fig. 5 shows the wave velocity and dissipation factor as a function of gas saturation for three values of the clay content and 35 Hz. Attenuation decreases with increasing clay content. Since the permeability of the medium is 0.15 D, 0.04 D and 0.012 D for $C = 0.2$, 0.4 and 0.7, respectively, decreasing permeability moves the mesoscopic relaxation peak to the low frequencies outside the exploration frequency band (see Eq. (7.449) in Carcione (2015) for the expression of the peak frequency). This effect can be seen in Fig. 6, where the seismic properties are represented as a function of frequency for a gas saturation of 8%. Fig. 7 shows the same properties for a clay content of 40% and different gas saturations. In this case, the peak moves to higher frequencies with increasing gas saturation. As can be seen in these plots, the interpretation is not intuitive and a proper rock-physics model is essential to reach valid conclusions about the influence of the different parameters (clay content, frequency, saturation, etc.) on the wave properties. The full waveform is displayed in Fig. 8, where (a) $C = 0.4$ and (b) $S_g = 8\%$. The solid curve in (a) and (b) is the same seismic trace, while the dashed curve in (a) corresponds to $S_g = 0.02$ and the dashed curve in (b) corresponds to $C = 0.2$. At $S_g = 8\%$ the attenuation of the layer is higher than at $S_g = 2\%$ (see Fig. 5b) and this fact explains that the event reflected from the interface below the BSR at 0.7 is more damped (see Fig. 8a). Similarly, since at $C = 0.2$ the attenuation of the layer is higher than at $C = 0.4$ (Fig. 5b), this event is more attenuated (see Fig. 8b). However the event coming from the BSR is in both cases stronger. This shows that the effects can be counterintuitive and modeling is required.

Finally, we quantify the effects of overburden. The average Q

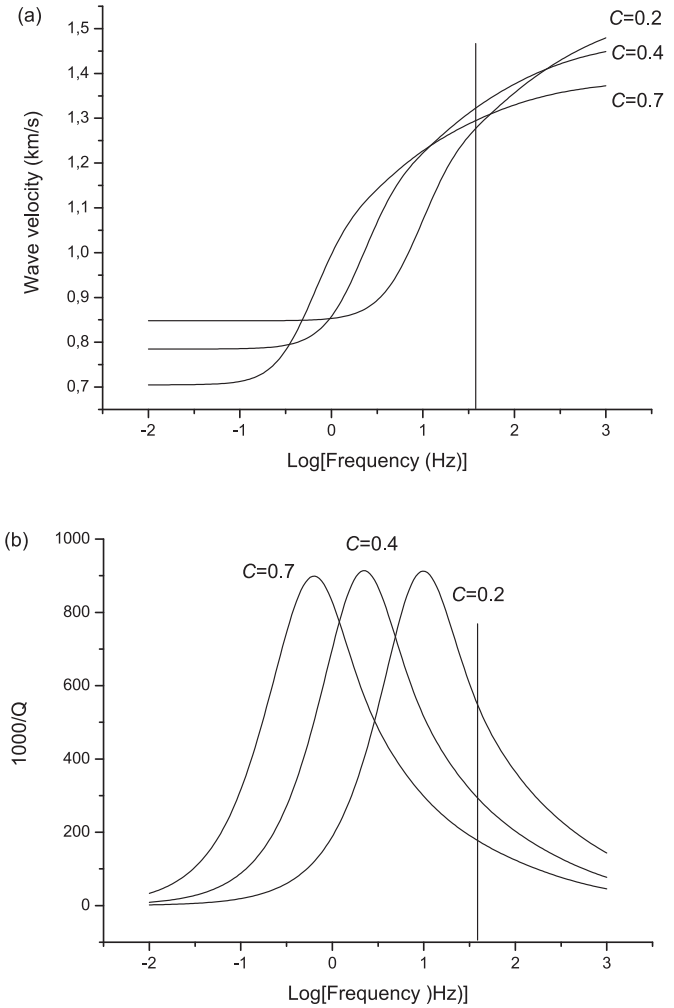

Fig. 6. Wave velocity (a) and quality factor (b) as a function of frequency for a gas saturation of 8%. The vertical line indicates 35 Hz.

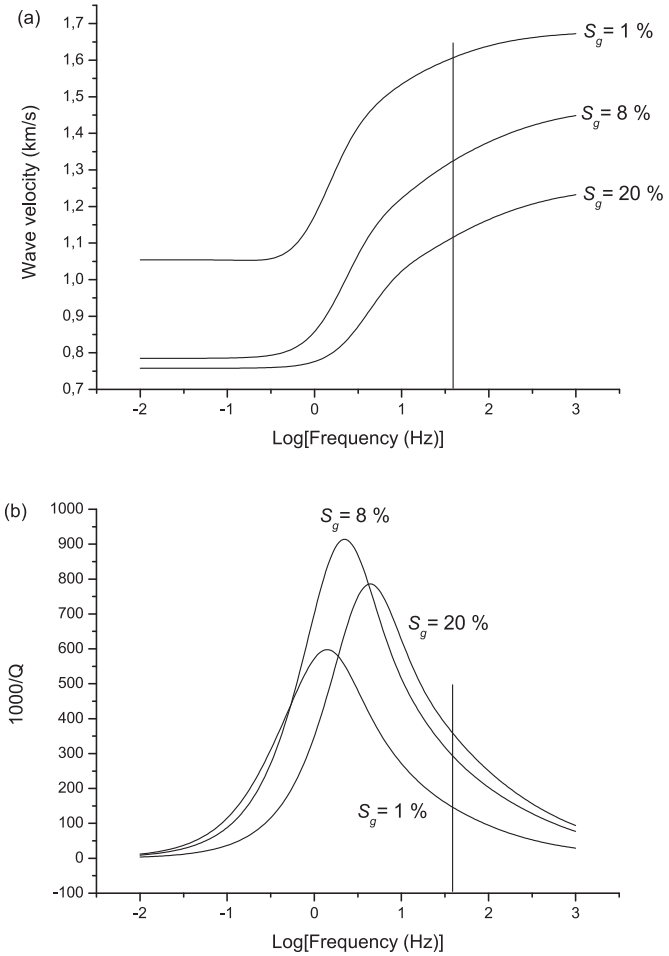

Fig. 7. Wave velocity (a) and quality factor (b) as a function of frequency for a clay content of 40%. The vertical line indicates 35 Hz.

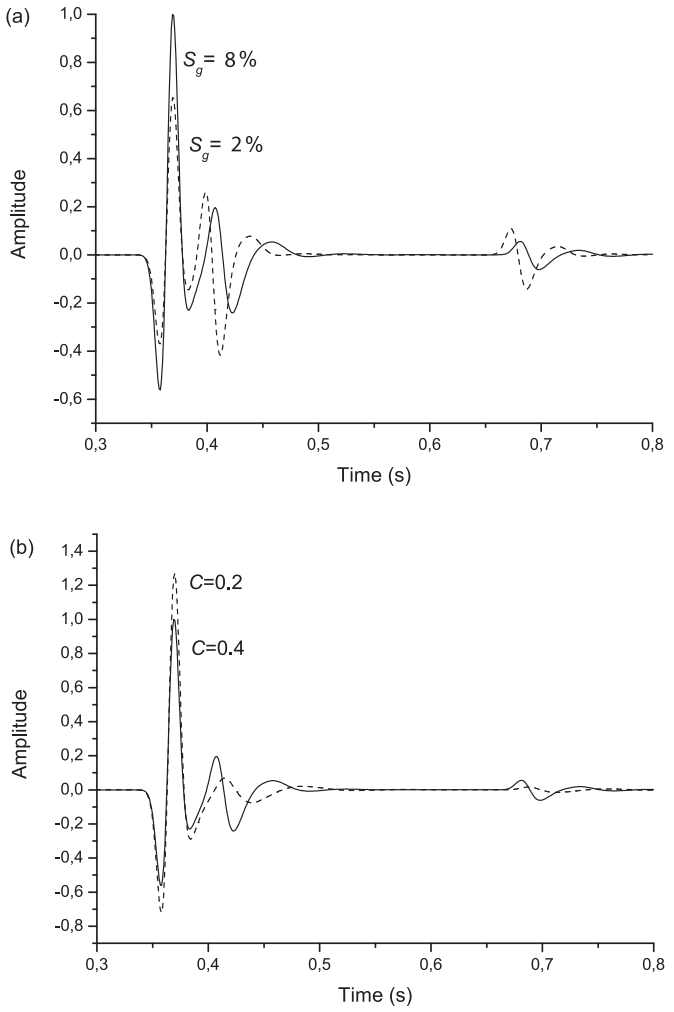

Fig. 8. Full waveforms, where (a) $C = 0.4$ and (b) $S_g = 0.08$. The solid line in (a) and (b) is the same seismic trace, while the dashed line in (a) corresponds to $S_g = 0.02$ and the dashed line in (b) corresponds to $C = 0.2$. The thickness of the layer is $h = 30$ m and the signal frequency is 35 Hz.

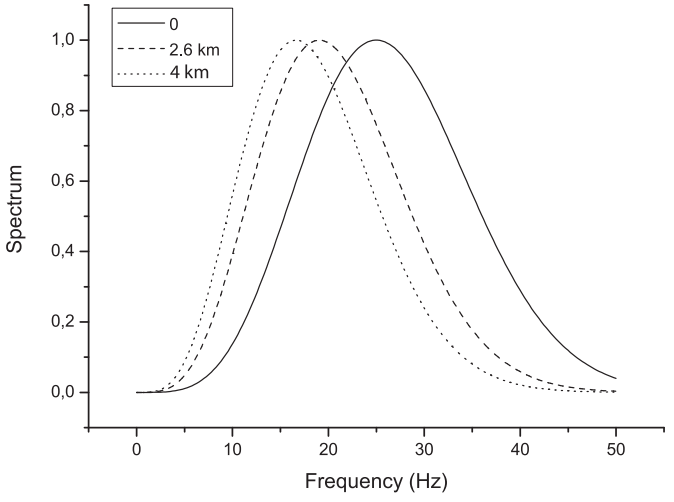

Fig. 9. Spectra of the signal as a function of source-receiver distance for the reflection event corresponding to the BSR layer. Changes are due to intrinsic attenuation of the upper layers. The curves are normalised with respect to that of zero distance. The maximum amplitudes are 1 (0 km), 0.2 (2.6 km) and 0.07 (4 km).

factor of a sequence of N layers of thickness h_i and quality factor Q_i is given in Appendix B, Equation (26). At normal incidence and down to the BSR layer, the average quality factor is $Q = 117$, with an average velocity $v = 1596$ m/s and a two-way propagation distance of 2.6 km at normal incidence (with values given in Fig. 1 and Table 1). We then assume a larger distance of 4 km for comparison. In Appendix C we show how the centroid f_c of the spectrum of a signal moves as a function of the traveled distance due to intrinsic attenuation. The damping values, represented by the exponential decay (see Equation (28)), are 0.33 and 0.18, respectively. Fig. 9 shows the spectra of the signal as a function of traveled distance, where we have assumed a source peak frequency of 25 Hz. The centroids are 26.4 Hz, 20.9 Hz and 18.6 Hz at the source location, 2.6 km and 4 km, respectively. Hence, there is a frequency shift of approximately 8 Hz for a distance of 4 km, due to the loss of high frequencies by intrinsic attenuation in the upper layers.

6. Conclusions

We propose a simple 1D methodology to analyze the seismic response of a BSR layer, based on rock physics and numerical modeling, focused mainly on the effects of intrinsic loss. The model is based on poroelasticity and the modeling provides the full wavefield. Quantities such as signal frequency, clay content, porosity, permeability, hydrate concentration and fluid saturation, in addition to the thicknesses of the various layers involved in the system, can be varied to study their effects on the seismic properties (velocity and attenuation) and on the waveform of the reflection events. Moreover, the effects of the overburden due to attenuation are quantified.

The results show that many of the effects can be counterintuitive, indicating that proper rock-physics modeling is essential. The dimensionality of the space (2D, 3D) can add more geometrical and physical effects that can make the problem more complicated. An example is offset effects due to NMO processing and intrinsic loss. It is known that NMO stretching removes high frequency components of the signal and this can be confused with intrinsic attenuation effects. This and other features related to the BSR problem, will be tackled in a future work.

Appendix A. List of symbols

α	Attenuation factor.
c	Complex velocity.
c_p	Phase Velocity.
e	Memory variable.
Φ	Porosity.
f	Frequency.
g	Source time history.
h	Layer thickness.
k	Wavenumber.
K	Bulk modulus.
μ	Shear modulus.
Q	Quality factor.
R	Reflection coefficient.
P	Mass density.
σ	Stress.
τ	Relaxation time.
t	Traveltime.
v_z	Particle velocity.
ω	Angular frequency.
X	Spatial distance.
Z	Seismic impedance.

Appendix B. Time–average equation for the quality factor

Wyllie et al. (1956) obtained the so-called time average equation, which they applied to porous media. A similar version can be used to compute the average velocity of a stack of N layers

$$v = \left(\frac{1}{h}\sum_{i=1}^{N}\frac{h_i}{v_i}\right)^{-1}, \quad h = \sum_{i=1}^{N} h_i \tag{21}$$

(e.g., Carcione, 2015), where h_i is the thickness of the ith layer and v_i is its phase velocity.

Here we obtain a similar equation to obtain an average quality factor of the stack of layers. Consider that the N layers have quality factors Q_i, $i = 1,\ldots,N$. A plane wave in a lossy medium attenuates as

$$\prod_{i=1}^{N}\exp(-\alpha_i h_i) \approx \prod_{i=1}^{N}\exp\left(-\frac{\omega}{2v_iQ_i}h_i\right), \tag{22}$$

(e.g., Carcione, 2015), where α_i is the attenuation factor. We may rewrite (22) as

$$\exp\left(-\frac{\omega}{2}\sum_{i=1}^{N}\frac{h_i}{v_iQ_i}\right), \tag{23}$$

or

$$\exp\left(-\frac{\omega h}{2vQ}\right), \tag{24}$$

where

$$Q = \left(\frac{v}{h}\sum_{i=1}^{N}\frac{h_i}{v_iQ_i}\right)^{-1} \tag{25}$$

is the average quality factor. Note that if we define the traveltime of each layer as $t_i = h_i/v_i$, the average or equivalent quality factor is

$$Q = \sum_{i=1}^{N} t_i \Big/ \sum_{i=1}^{N}\frac{t_i}{Q_i}, \tag{26}$$

i.e., the weighted average of the single Q factors where the weighs are the transit times.

Appendix C. Centroid of the signal spectrum

The 1D wavefield displacement in a viscoelastic medium is given, for instance, in Carcione et al. (2010):

$$U(\omega, x) = G(\omega)\exp(-\mathrm{i}kx), \tag{27}$$

where G is the source spectrum and k is the complex wavenumber. The power spectrum is

$$P(\omega) = |U(\omega)|^2 = |G|^2\exp(-2\alpha x), \tag{28}$$

where

$$G(\omega) = \left(\frac{t_p}{\sqrt{\pi}}\right)o\exp(-o - \mathrm{i}\omega t_s), \quad o = \left(\frac{\omega}{\omega_p}\right)^2, \quad \omega_p = 2\pi f_p, \tag{29}$$

obtained as the Fourier transform of (20), and α is given by Equation (10).

The centroid frequency of the power spectrum when the signal has traveled the distance x is then

$$f_c(x) = \frac{\int_0^\infty \omega P(\omega, x)d\omega}{2\pi\int_0^\infty P(\omega, x)d\omega} = \frac{\int_0^\infty \omega|G|^2\exp(-2\alpha x)d\omega}{2\pi\int_0^\infty |G|^2\exp(-2\alpha x)d\omega}. \tag{30}$$

References

Born, M., Wolf, E., 1964. Principles of Optics. Pergamon Press, Oxford.

Brekhovskikh, L.M., 1960. Waves in Layered Media. Academic Press Inc.

Brie, A., Pampuri, F., Marsala, A.F., Meazza, O., 1995. Shear Sonic Interpretation in Gas-bearing Sands. SPE Annual Technical Conf., nr. 30595, pp. 701–710.

Carcione, J.M., 2015. Wave Fields in Real Media. Theory and Numerical Simulation of Wave Propagation in Anisotropic, Anelastic, Porous and Electromagnetic Media, third ed. Elsevier.

Carcione, J.M., Gei, D., 2004. Gas hydrate concentration estimated from P- and S-wave velocities at the Mallik 2L-38 research well, Mackenzie Delta, Canada. J. Appl. Geophys. 56, 73–78.

Carcione, J.M., Gei, D., Rossi, G., Madrussani, G., 2005a. Estimation of gas hydrate concentration and free-gas saturation at the Norwegian-Svalbard continental margin. Geophys. Prospect. 53, 803–810.

Carcione, J.M., Gei, D., Picotti, S., Michelini, A., 2012. Cross-hole electromagnetic and seismic modeling for CO_2 detection and monitoring in a saline aquifer. J. Pet. Sci. Eng. 100, 162–172.

Carcione, J.M., Gei, D., Treitel, S., 2010. The velocity of energy through a dissipative medium. Geophysics 75, T37–T47.

Carcione, J.M., Helle, H.B., Santos, J.E., Ravazzoli, C.L., 2005b. A constitutive equations and generalized Gassmann modulus for multi-mineral porous media. Geophysics 70, N17–N26.

Carcione, J.M., Picotti, S., 2006. P-wave seismic attenuation by slow-wave diffusion. Effects of inhomogeneous rock properties. Geophysics 71, O1–O8.

Carcione, J.M., Robinson, E., 2002. On the acoustic-electromagnetic analogy for the reflection-refraction problem. Stud. Geophys. Geod. 46, 321–345.

Carcione, J.M., Tinivella, U., 2000. Bottom simulating reflectors: seismic velocities and AVO effects. Geophysics 65, 54–67. Errata: 2001, 66, 984.

Dewangan, P., Mandal, R., Jaiswal, P., Ramprasad, T., Sriram, G., 2014. Estimation of seismic attenuation of gas hydrate bearing sediments from multi-channel seismic data: a case study from Krishna-Godavari offshore basin. Mar. Pet. Geol. 58, 356–367.

Dunkin, J.W., Levin, F.K., 1973. Effects of normal moveout on a seismic pulse. Geophysics 38, 635–642.

Gei, D., Carcione, J.M., 2003. Acoustic properties of sediments saturated with gas hydrate, free gas and water. Geophys. Prospect. 51, 141–157.

Geletti, R., Busetti, M., 2011. A double bottom simulating reflector in the western Ross sea (Antarctica). J. Geophys. Res. 116, B04101. http://dx.doi.org/10.1029/2010JB007864.

Makogon, Y.F., 2010. Natural gas hydrates – a promising source of energy. J. Nat. Gas Sci. Eng. 2, 49–59.

Mavko, G., Mukerji, T., Dvorkin, J., 1998. The Rock Physics Handbook: Tools for Seismic Analysis in Porous Media. Cambridge University Press, Cambridge, UK.

Müller, T., Gurevich, B., Lebedev, M., 2010. Seismic wave attenuation and dispersion resulting from wave-induced flow in porous rocks – a review. Geophysics 75, A147–A164.

Rossi, G., Gei, D., Böhm, G., Madrussani, G., Carcione, J.M., 2007. Attenuation tomography: an application to gas-hydrate and free-gas detection. Geophys. Prospect. 55, 655–669.

Taylor, M.H., Dillon, W.P., Pecher, I.A., 2000. Trapping and migration of methane associated with the gas hydrate stability zone at the Blake Ridge Diapir: new insights from seismic data. Mar. Geol. 164, 79–89.

Vanneste, M., De Batist, M., Golmshtok, A., Kremlev, A., Versteeg, W., 2001. Multi-frequency seismic study of gas hydrate-bearing sediments in Lake Baikal, Siberia. Mar. Geol. 172, 1–21.

White, J.E., 1975. Computed seismic speeds and attenuation in rocks with partial gas saturation. Geophysics 40, 224–232.

Wyllie, M.R.J., Gregory, A.R., Gardner, L.W., 1956. Elastic wave velocities in heterogeneous and porous media. Geophysics 21, 41–70.